American Mineralogist, Volume 109, pages 449–456, 2024

Equation of state and structural evolution of manganese dolomite (kutnohorite) under high pressures

Liangxu Xu[1], Weibin Gui[1], Kewei Shen[1,*], Dongzhou Zhang[2,†], Jingui Xu[3], and Jin Liu[4,*,‡]

[1]Center for High Pressure Science and Technology Advanced Research, Beijing 100193, China
[2]Center for Advanced Radiation Sources, University of Chicago, Chicago, Illinois 60439, U.S.A.
[3]Institute of Geochemistry, Chinese Academy of Sciences, Guiyang, Guizhou 550002, China
[4]Center for High Pressure Science, State Key Laboratory of Metastable Materials Science and Technology, Yanshan University, Qinhuangdao 066004, China

Abstract

Understanding the structural evolution of carbonate minerals with increasing pressure is essential to decoding the role of Earth's mantle in the global carbon cycle and long-term climate change. Here, we carried out synchrotron single-crystal X-ray diffraction measurements on a natural sample of manganese dolomite [kutnohorite, $Ca_{1.11}Mn_{0.89}(CO_3)_2$] in a diamond-anvil cell up to 51.2 GPa at room temperature with neon as the pressure-transmitting medium. The manganese dolomite sample remains stable in the rhombohedral structure from 1 bar to ~13.3 GPa. The equation of state of $Ca_{1.11}Mn_{0.89}(CO_3)_2$ was determined: V_0 = 334.06 ± 0.29 Å^3, K_0 = 99.9 ± 4.7 GPa, and K_0' = 4.3 ± 0.9; when K_0' is fixed at 4.0, V_0 = 334.04 ± 0.24 Å^3, and K_0 = 101.4 ± 1.5 GPa. Upon further compression at room temperature, the split and disappearance of diffraction spots were observed. That is, the rhombohedral structure of manganese dolomite becomes highly distorted to lose its long-range order at 13.3–51.2 GPa at room temperature. Moreover, our single-crystal X-ray diffraction results reveal the mechanisms of the reported lattice and internal Raman mode splits of the same manganese dolomite sample approximately at 13 and 24 GPa, respectively. These results suggest manganese-bearing carbonates may play a distinct role in the deep carbon cycle.

Keywords: High pressure, manganese dolomite, X-ray diffraction, deep carbon cycle; Physics and Chemistry of Earth's Deep Mantle and Core

Introduction

Carbonate minerals are the important forms of carbon carriers from shallow subduction zones to the deep mantle (Plank and Manning 2019). Those carbonate minerals could account for the major constituent of the global carbon fluxes, with about 100 megatons of deep carbon entering the Earth's interior via subducting slabs each year (Dasgupta and Hirschmann 2010; Farsang et al. 2021). Little to no carbon can be incorporated into the crystal lattice of mantle silicate minerals, leading to the deep carbon being mostly stored and transported as carbonates, together with graphite, diamond, and carbides (Shcheka et al. 2006). The physical, chemical, and transport properties of the deep mantle could be significantly influenced by the presence of carbonates involving the crust-mantle interactions (Lavina et al. 2009; Lin et al. 2012; Dorfman et al. 2018). In particular, it remains enigmatic how those carbonate minerals evolve in subducted slabs. This holds the key to better decoding the global carbon cycle, long-term climate dynamics, as well as mantle dynamics (Kelemen et al. 2011; Sanchez-Valle et al. 2011; Malusà et al. 2018).

Thus far, the structural evolution and chemical reactions of carbonate minerals have been investigated by a battery of probes under high-pressure and high-temperature conditions (e.g., Boulard et al. 2011; Zhao et al. 2020). Calcium carbonate (e.g., calcite and aragonite) could react with pyroxene to form the dolomite group minerals [$CaM(CO_3)_2$ with M = Mg, Fe, Mn, etc.] under relatively shallow depths of 100–150 km (Kushiro 1975). Dolomite minerals exhibit a rhombohedral structure (space group $R\bar{3}$) in which MO_6 and CaO_6 units alternate along the *c*-axis. The dolomite group minerals undergo a series of high-pressure phase transformations including dolomite-II, -III, -IIIc, -IV, and -V (e.g., Santillán et al. 2003; Mao et al. 2011; Merlini et al. 2012, 2017; Wang et al. 2022). Dolomite minerals and their high-pressure polymorphs likely occupy up to half of the Earth's accessible carbonate reservoirs (Binck et al. 2020). Among all the dolomite group minerals investigated under high pressures, the high-pressure behavior of manganese dolomite [$CaMn(CO_3)_2$] is the least constrained in the literature. Palaich et al. (2015) reported the bulk modulus and phase stability of a natural manganese dolomite sample [$Ca_{0.76}Mn_{1.24}(CO_3)_2$] (hereinafter referred to as "Ca76") in the Ne-NaCl pressure-transmitting medium. Notably, varying pressure-transmitting media (e.g., NaCl, Ar, Ne, and He) can have distinct effects on the structural transition paths and electronic states with increasing pressure (Efthimiopoulos et al. 2017, 2019; Merlini et al. 2017; Binck et al. 2020; Zhao et al. 2021). The use of NaCl generally induces a very large deviatoric stress of >5–10 GPa in a diamond-anvil cell (DAC), whereas Ne can keep the sample under relatively hydrostatic conditions that more closely resemble the deep mantle (Klotz et al. 2009).

* Co-corresponding authors E-mail: jinliuyc@foxmail.com, kewei.shen@hpstar.ac.cn
† Orcid 0000-0002-6679-892X
‡ Special collection papers can be found online at http://www.minsocam.org/MSA/AmMin/special-collections.html.

0003-004X/24/0003–449$05.00/DOI: https://doi.org/10.2138/am-2023-8949

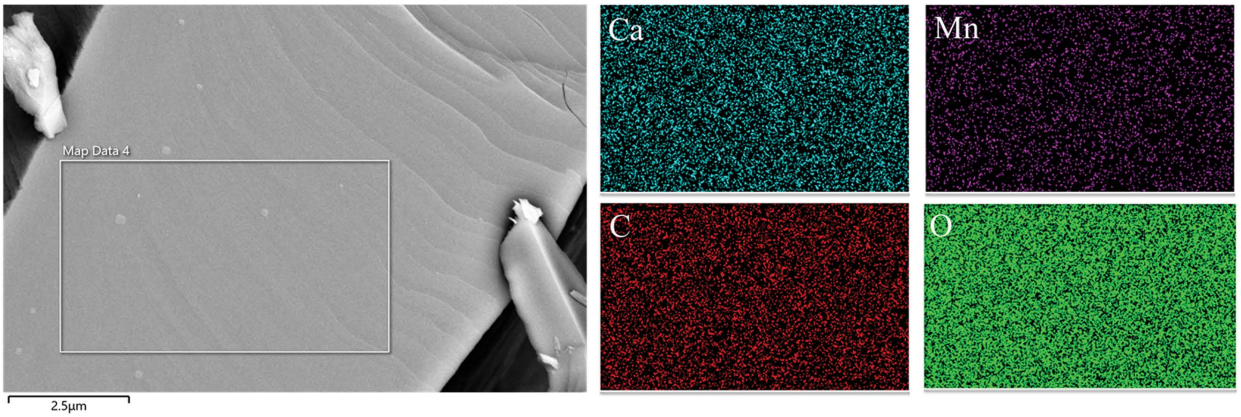

Figure 1. Representative backscattered electron image and energy-dispersive X-ray spectroscopy (EDS) elemental maps (Ca, Mn, C, and O) of manganese dolomite at ambient conditions. (Color online.)

It is noted that the ideal manganese dolomite $CaMn(CO_3)_2$ (hereinafter referred to as "Ca100") may feature separated CaO_6 and MnO_6 layers alternating along the *c* axis. Compared with the Ca100, the Ca76 has a lower calcium content and features CaO_6 and MnO_6 octahedra mixed in the same layer (Palaich et al. 2015). That is, varying manganese contents would change the degree of cation ordering in manganese dolomite minerals. In particular, the different sizes between Mn^{2+} and Ca^{2+} would induce rotation and distortion of the CaO_6 and MnO_6 octahedra in the same layer to some extent, which definitely influences the manganese dolomite's stability under high pressures. Therefore, manganese content shall also be evaluated for constraining the structural transformation of manganese dolomite under Earth's mantle pressures.

In this work, we carried out synchrotron X-ray diffraction measurements on a natural single-crystal manganese dolomite mineral $Ca_{1.11}Mn_{0.89}(CO_3)_2$ (hereinafter referred to as "Ca111") under high pressures up to 51.2 GPa at room temperature. Our manganese dolomite sample has a calcium content slightly deviating from the ideal manganese dolomite (Ca100). Using neon as the pressure-transmitting medium, this study aims to investigate how varying chemical compositions influence the structural evolution of manganese dolomite under high pressures. It is found that our Ca111 sample exhibits enhanced incompressibility with respect to the Ca76 sample reported by Palaich et al. (2015). Upon further compression at room temperature, a new set of splitting diffraction spots emerged at pressures greater than 13.3 GPa, including {110}, {116}, and {128} planes. Meanwhile, the intensity of the splitting diffraction spots diminished approximately from 22.4 to 51 GPa, suggesting that the manganese dolomite structure becomes highly distorted at >13.3 GPa and partially loses the long-range order at >22.4 GPa at room temperature. These results provide a better understanding of the structural behavior of manganese-bearing carbonates at mantle pressures.

Experimental methods

The starting material was a single-crystal Ca111 sample, one natural manganese dolomite (i.e., kutnohorite) from Sterling Hill, New Jersey, U.S.A.. Backscattered electron images and elemental maps (Ca, Mn, C, and O) were collected for the Ca111 sample using scanning electron microscopy/energy-dispersive X-ray spectroscopy (SEM/EDS, JOEL JSM-7900F). The accelerating voltage is 10 kV with a beam current of 10 nA. The Ca111 sample was coated with Pt. The chemical homogeneity of the starting material was confirmed, as illustrated in Figure 1. High-pressure Raman spectroscopy of this sample had been investigated up to 56 GPa by Wang et al. (2022), and the chemical composition of this sample was determined to be $Ca_{1.11}Mn_{0.89}(CO_3)_2$ with minor trace amounts of Mg and Fe using electron probe microanalyzer (JEOL JXA-8200). In addition, the rhombohedral structure (space group: $R\bar{3}$) was confirmed for the Ca111 sample with lattice parameters of a = 4.8644 ± 0.0010 Å, c = 16.294 ± 0.003 Å, and the unit-cell volume V = 333.90 ± 0.15 Å^3, using an in-house single-crystal X-ray diffractometer (Brucker D8 VENTURE) at the Center for High Pressure Science and Technology Advanced Research (HPSTAR, Beijing). The diffractometer was equipped with a Mo$K\alpha$ X-ray source and operated at a voltage of 50.0 kV with a current of 1.4 mA and a wavelength of 0.71073 Å. The X-ray beam was focused to the full-width at half maximum (FWHM) of ~100 µm at the sample position, and the diffraction patterns were collected using a MAR CCD detector. The X-ray diffraction patterns of CeO_2 powder were collected for the calibration of laboratory X-ray diffractometer.

Symmetric diamond-anvil cells were employed to generate high pressures by squeezing the two opposing diamond anvils with a flat culet of 200 µm. A hole of 110 µm in diameter and 22–25 µm thick was drilled at the center of a pre-indented tungsten gasket and served as a sample chamber. A small platelet of the single-crystal Ca111 sample was deliberately selected with a thickness of 7–8 and 40–45 µm in diameter, and then it was loaded into the sample chamber. One ruby ball of 7–8 µm in diameter and a piece of platinum foil of ~15 µm in diameter were placed next to the Ca111 sample for pressure calibration. Neon was employed as a pressure-transmitting medium and loaded into the sample chamber by using the high-pressure gas loading system at HPSTAR. The use of neon can ensure the quasi-hydrostatic conditions at least up to 50 GPa, avoiding the influence of severe deviatoric stress inside the sample chamber (Klotz et al. 2009). The pressure and its uncertainty were calculated by multiple measurements of the ruby fluorescence before and after each X-ray diffraction measurement, together cross-checked by the equation of state (EOS) of platinum under high pressures at room temperature (Fei et al. 2007; Shen et al. 2020).

High-pressure single-crystal X-ray diffraction experiments were performed at beamline 13BM-C of the GeoSoilEnviroCARS (GSECARS) at the Advanced Phonon Source, Argonne National Laboratory. A monochromatic X-ray beam was employed with a wavelength of 0.4340 Å. The incident X-ray beam was focused down to 15 µm at the full width at half maximum on the sample position. A MAR165 CCD detector was used to record X-ray diffraction images while the sample was rotated from –19° to +20° about the X-ray beam direction for a total exposure time of 10 s. In addition, lanthanum hexaboride (LaB_6) powder was used to calibrate the sample-to-detector distance and the tilting and rotation of the image plate with respect to the incident X-ray beam. The sample-to-detector distance was calibrated to be 208.20 mm, and X-ray diffraction patterns were processed to determine the lattice parameters of the Ca111 sample and platinum (pressure calibrant) with increasing pressure using the GSE_ADA/RSV software packages and Dioptas software (Dera et al. 2013; Prescher and Prakapenka 2015).

Results and discussion

Synchrotron X-ray diffraction patterns were collected on the single-crystal Ca111 sample at room temperature up to 51.2 GPa via an interval of ~2–10 GPa. At 1.9 GPa, 10 sets of diffraction planes were recorded at the *d*-spacing values ranging from 4.0650 to 1.2135 Å, including {104}, {110}, {202}, {116}, {210}, {214}, {208}, {0210}, {128}, and {220} planes (Fig. 2a). The *d*-spacing values of these planes systematically decreased with increasing pressure while their diffraction spots shifted to higher degrees in X-ray diffraction patterns. Notably, all these diffraction spots remained pretty sharp and round under high pressures up to 13.3 GPa, indicating that the Ca111 sample was in good single-crystal quality in neon pressure medium (Fig. 2b). Upon further compression, the diffraction spots became elongated and split at pressures greater than 13.3 GPa (Fig. 2c). The dramatic decline in diffraction intensity was observed at >22.4 GPa, largely due to the fact that the Ca111 sample underwent octahedral distortion/rotation to lose its long-range order, which has also been reported in Ca-Mg dolomite under high pressures (Santillán et al. 2003). This suggests the manganese dolomite symmetry is broken approximately at >13.3–22.4 GPa and room temperature. This is consistent with the previous Raman spectroscopic study on the same Ca111 sample at room temperature, revealing several new *T* and *L* Raman modes of 150–450 cm^{-1} at ~13 GPa and the splitting of the ν_1 mode at ~23–25 GPa (Wang et al. 2022).

The pressure-volume (*P*-*V*) experimental data between 1 bar and 13.3 GPa were fitted to the third-order Birch-Murnaghan equation of state (EoS) (Table 1; Fig. 3):

$$P = \frac{3}{2}K_0\left[\left(\frac{V_0}{V}\right)^{\frac{7}{3}} - \left(\frac{V_0}{V}\right)^{\frac{5}{3}}\right]\left\{\left[1 + \frac{3}{4}\left(K_0' - 4\right)\left(\left(\frac{V_0}{V}\right)^{\frac{2}{3}} - 1\right)\right]\right\}$$

where *P* is pressure, V_0 and K_0 are the unit-cell volume (*V*) and bulk modulus (*K*) at ambient conditions, respectively, and K_0' is the pressure derivative of K_0. With all the parameters fitted, we derived V_0 = 334.06 ± 0.29 Å^3, K_0 = 99.9 ± 4.7 GPa, and K_0' = 4.3 ± 0.9 for the Ca111 sample; with the V_0 fixed at the value of 333.90 Å^3 measured at ambient conditions, the K_0 and K_0' values were calculated to be 101.8 ± 3.4 GPa and 4.1 ± 0.6, respectively; with the K_0' fixed at 4.0, V_0 = 334.04 ± 0.24 Å^3, and K_0 = 101.4 ± 1.5 GPa. Note that the *P*-*V* experimental data at >13.3 GPa were not included for deriving the EoS of the Ca111 sample here due to the splits of diffraction spots (Table 1).

Compared to the Ca76 sample reported by Palaich et al. (2015), the unit-cell volume of our Ca111 sample is greater over the entire pressure range. Their Ca76 data exhibit a clear scat-

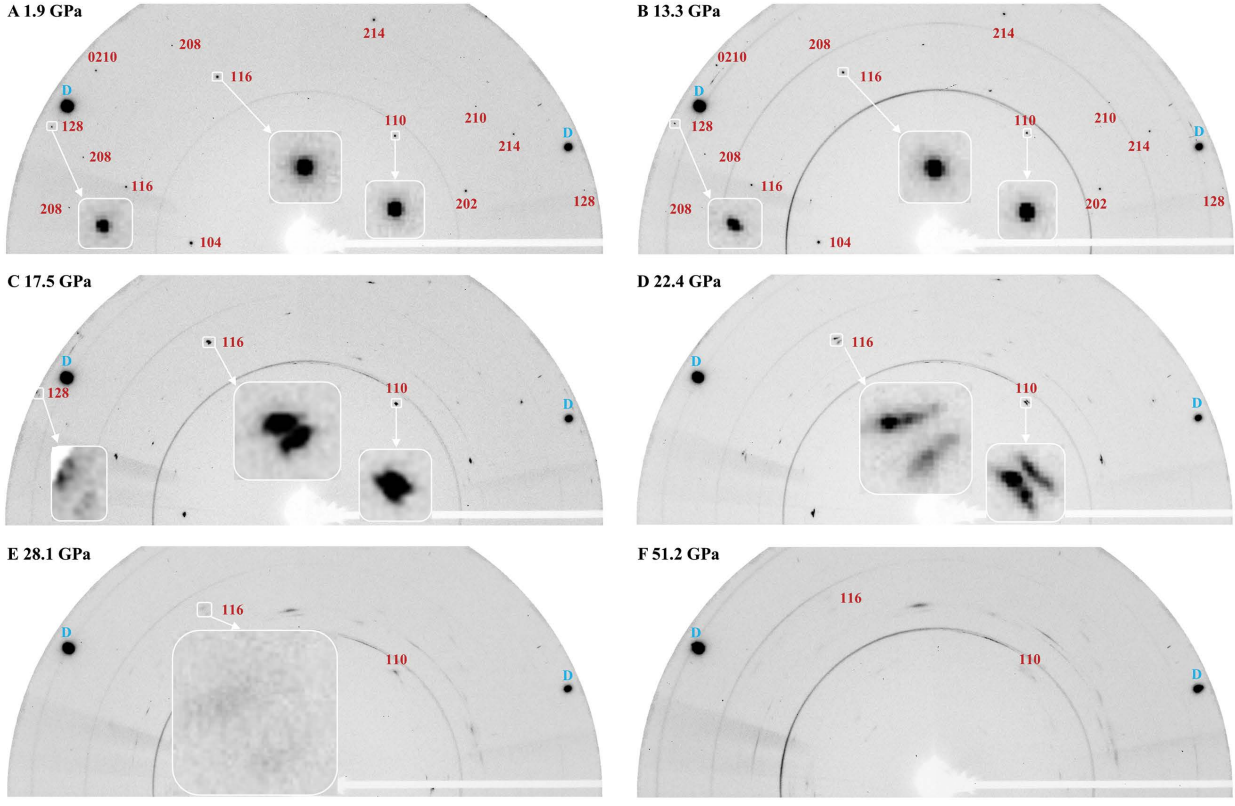

Figure 2. Representative X-ray diffraction patterns of manganese dolomite under high pressures at ambient temperature. X-ray diffraction images collected during a rotation from –19° to +20° about the X-ray beam direction showing the sharp, round diffraction spots of $Ca_{1.11}Mn_{0.89}(CO_3)_2$ at 1.9 and 13.3 GPa, respectively. The diffraction rings in the aforementioned patterns come from the tungsten gasket, the pressure calibrant of platinum, and/or the pressure medium of neon. The diffraction images were illustrated by the DIOPTAS program (Prescher and Prakapenka 2015). The symbol D represents the diffraction spots of diamond anvils. Insets: The enlarged images of diffraction spots by 10 times vertically and horizontally, respectively. (Color online.)

Table 1. Lattice parameters of $Ca_{1.11}Mn_{0.89}(CO_3)_2$ and the pressure calibrant (platinum) at high pressure and room temperature with the use of neon as a pressure-transmitting medium

$Ca_{1.11}Mn_{0.89}(CO_3)_2$			Pt		
a (Å)	*c* (Å)	*V* (Å³)	*a* (Å)	*V* (Å³)	*P* (GPa)[a]
4.8644(10)	16.294(3)	333.90(15)	3.9231(3)	60.379(14)	0.0001
4.8517(10)	16.121(7)	328.63(20)	3.9143(5)	59.974(23)	1.9(1)
4.8149(11)	15.735(9)	315.92(23)	3.8967(8)	59.169(36)	6.0(2)
4.8058(9)	15.613(7)	312.28(18)	3.8892(8)	58.828(36)	7.7(2)
4.7973(10)	15.547(7)	309.85(19)	3.8843(12)	58.605(54)	8.9(3)
4.7877(9)	15.443(7)	306.56(18)	3.8779(21)	58.316(95)	10.5(5)
4.7763(11)	15.355(8)	303.36(21)	3.8717(20)	58.037(90)	12.1(5)
4.7677(10)	15.286(8)	300.92(20)	3.8671(15)	57.830(67)	13.3(4)
4.7569(11)[b]	15.161(8)[b]	297.11(21)[b]	3.8618(11)	57.593(49)	14.7(3)
4.7523(11)[b]	15.101(8)[b]	295.36(21)[b]	3.8589(14)	57.463(63)	15.5(4)
4.7409(13)[b]	15.015(9)[b]	292.27(24)[b]	3.8564(18)	57.352(80)	16.2(5)
–	–	–	3.8517(12)	57.142(53)	17.5(3)

Notes: The digits in parentheses are the uncertainty, to the precision of the same number of least significant digits.
[a] The pressure was determined according to platinum's equation of state reported by Fei et al. (2007).
[b] These values should be used with caution because of diffraction splits.

ter above 15 GPa; hence, we refitted their data at 0.4–11.4 GPa using a third BM EoS and derived the V_0, K_0, and K_0' values to be 331.88(27) Å³, 93.4(77) GPa and 2.7(1.5), respectively; with the K_0' fixed at 4.0, the V_0 and K_0 values are 332.03(19) Å³ and 87.4(13) GPa, respectively. The bulk modulus of the Ca76 sample is consistently smaller than that of our Ca111 sample, evidencing that the Ca76 is more compressible than the Ca111 under high pressures. However, this observation is counterintuitive because our Ca111 sample contains much more Ca^{2+} than the Ca76. It is expected that the Ca111 is more compressible than the Ca76 on the basis of comparative crystal chemistry (Hazen et al. 2000). This contradiction might be resolved by the fact that the Ca111 sample is closer to the ideal composition of manganese dolomite

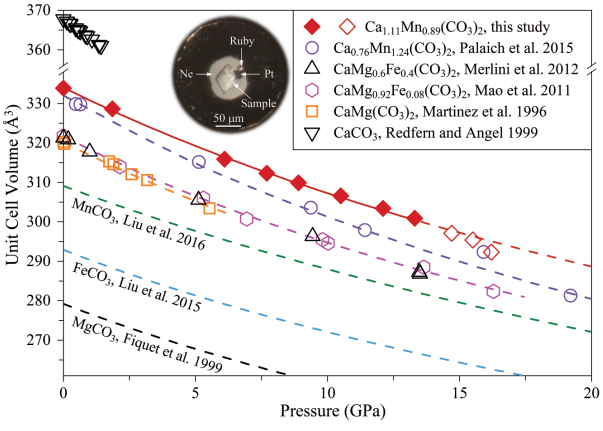

Figure 3. The pressure-volume relations of carbonate minerals at room temperature. Diamond symbols represent the unit-cell volume for $Ca_{1.11}Mn_{0.89}(CO_3)_2$ from this study while circle symbols for $Ca_{0.76}Mn_{1.24}(CO_3)_2$ by Palaich et al. (2015). Solid (red) and dashed (purple) curves: BM EoS fits to the experimental data of the two kutnohorite samples, respectively. Error bars smaller than diamond symbols are not shown for clarity for $Ca_{1.11}Mn_{0.89}(CO_3)_2$. Note that the open diamond symbols represent the values after diffraction splits, which should be used with caution (see Table 1 for more details). Inset: An optical microscopy image of the DAC sample chamber, showing that one ruby ball of 7–8 μm in diameter and a piece of platinum foil of ~15 μm in diameter were placed next to the sample for pressure calibration. (Color online.)

Ca100, while the Ca76 deviates from the ideal Ca100 composition to a greater degree. The Ca76 sample could accumulate larger lattice strain (i.e., microstrain) due to the greater rotation and distortion inside the cation layers at a given pressure and room temperature, originating from different sizes of CaO_6 and MnO_6 units in the same layer (Palaich et al. 2015). How Ca^{2+} and Mn^{2+} cations are arranged in the MO_6 layers reflects the degree of cation ordering, which should be highly associated with the calcium contents of manganese dolomite. The degree of cation ordering has also been frequently related to the phase stability of dolomite minerals. For instance, the ordered $CaMg(CO_3)_2$ enters the disordered state approximately at 620–1100 °C upon compression and further breaks down into $MgCO_3$ and $CaCO_3$ at higher pressures (Morlidge et al. 2006; Hammouda et al. 2011). The structural transformation and compressibility of carbonate minerals highly depend upon the degree of cation ordering. Additionally, it is worth noting that the stress field within the sample chamber might also contribute to the observed different compressibility between the Ca76 and Ca111 samples. Recently, it has been unraveled how the quasi- and non-hydrostatic conditions influence the structural evolution and compressibility of carbonate minerals as the pressure rises (Fiquet and Reynard 1999; Zhao et al. 2021).

The nature and state of carbonate minerals are largely related to the radii of cations (e.g., Ca^{2+}, Mg^{2+}, Fe^{2+}, and Mn^{2+}) under high pressures. Figure 3 and Table 2 show that calcite ($CaCO_3$) exhibits the largest unit-cell volume (V) and the least bulk modulus at ambient conditions among all single and double carbonate minerals with the chemical composition of $(Ca,Mn,Fe,Mg)CO_3$ (Redfern and Angel 1999; Redfern 2000). Intriguingly, rhodochrosite ($MnCO_3$) exhibits the greatest bulk modulus among all the $(Ca,Mn,Fe,Mg)CO_3$ carbonates, though its V value is much larger than siderite ($FeCO_3$) and magnesite ($MgCO_3$) at ambient conditions (Fiquet and Reynard 1999; Liu et al. 2015, 2016; Zhang et al. 1998). Moreover, the V values of the dolomite group minerals $CaM(CO_3)_2$ (M = Mn, Fe, and Mg) are in between rhodochrosite and calcite under high pressures (Fig. 3). Interestingly, $CaMg_{0.92}Fe_{0.08}(CO_3)_2$ and $CaMg_{0.6}Fe_{0.4}(CO_3)_2$ exhibit similar V values with increasing pressure (Martinez et al. 1996; Mao et al. 2011; Merlini et al. 2012). In other words, iron substitution appears to have minimal effects on the V of $CaMg(CO_3)_2$ at least up to 13 GPa at room temperature. However, manganese substitution presents distinct effects. The V values of the Ca76 and Ca111 are much larger than those of $CaMg(CO_3)_2$ under high pressures (Fig. 3). Unlike iron-bearing $CaMg(CO_3)_2$, the V values of manganese dolomite are highly related to manganese concentration. In general, manganese can more readily replace

Table 2. Bulk moduli of carbonate minerals at high pressure and room temperature

Carbonates	Bulk modulus (GPa)	References
$Ca_{1.11}Mn_{0.89}(CO_3)_2$	101.4(15)	This study
$Ca_{0.76}Mn_{1.24}(CO_3)_2$	85(6)	Palaich et al. (2015)
$CaMg(CO_3)_2$	90.7(7)	Martinez et al. (1996)
$CaMg_{0.918}Fe_{0.078}Mn_{0.016}(CO_3)_2$	94.1(4)	Mao et al. (2011)
$CaCO_3$	73.46(27)	Redfern and Angel (1999)
$MnCO_3$	122(3)	Liu et al. (2016)
$MgCO_3$	115(1)	Fiquet and Reynard (1999)
$FeCO_3$	117(1)	Zhang et al. (1998)

Notes: The digits in parentheses are the uncertainty, to the precision of the same number of least significant digits.

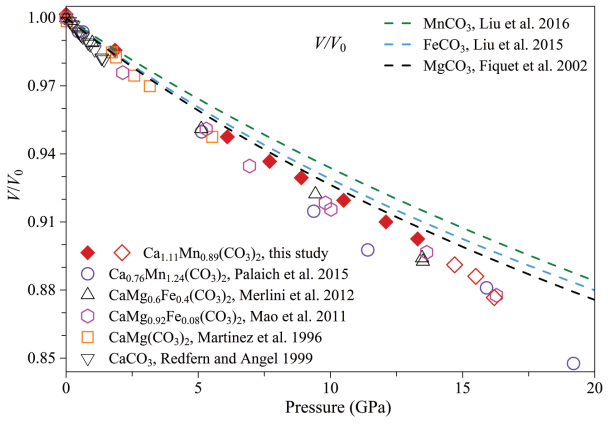

Figure 4. The V/V_0 values of carbonate minerals with increasing pressure at room temperature. Error bars smaller than symbols are not shown for clarity. Note that the open diamond symbols represent the values after diffraction splits of $Ca_{1.11}Mn_{0.89}(CO_3)_2$, which should be used with caution (see Table 1 for more details). (Color online.)

calcium in manganese dolomite, while iron mostly substitutes magnesium in Ca-Mg dolomite. This is largely because the radius of Ca^{2+} (1.00 Å) is much larger than that of Mg^{2+} (0.72 Å) and Fe^{2+} (0.78 Å in the high-spin state and 0.61 Å in the low-spin state) in the octahedral configuration (Shannon 1976).

Furthermore, the relative compressibility of carbonate minerals can be demonstrated evidently as a function of the V/V_0 ratio against pressure. Figure 4 shows the three features regarding how the V/V_0 ratio decreases with increasing pressure. First, all the single and double-divalent metal carbonates $(Ca,Mn,Fe,Mg)CO_3$ exhibit similar values that reach ~0.985 at 2 GPa, except calcite-type $CaCO_3$. Second, the single divalent metal carbonates of $(Mn,Fe,Mg)CO_3$ in the calcite-type structure have V/V_0 ratios greater than those of the double divalent metal carbonates of $(Ca,Mn,Fe,Mg)CO_3$ in the dolomite-type structure at >2 GPa. Third, the Ca111 sample has V/V_0 ratios greater than that of iron-bearing dolomite $CaMg(CO_3)_2$ at 0–13 GPa. These differences diminish with increasing pressure, and the Ca111, Ca76, and iron-bearing dolomite samples all could share the same V/V_0 ratios at ~15 GPa, as illustrated in Figure 4. Additionally, it is worth noting that the magnitude of deviation from the ideal calcium content of the Ca100 may control the evolution of V/V_0 and c/c_0 ratios of manganese dolomite minerals with increasing pressure, as shown in Figures 4–5 (Palaich et al. 2015). On the contrary, the a/a_0 ratios between the Ca76 and Ca111 samples are almost the same as the pressure rises (Fig. 5). More importantly, all the single and double carbonate minerals share comparable a/a_0 ratio values under high pressures. In other words, all these carbonates have a similar response of the *a*-axis upon compression. It is primarily because of the relatively rigid CO_3^{2-} planar configurations aligning perpendicular to the *c*-axis. Therefore, the type and size of MO_6 octahedra have little influence on the *a* axial compressibility of carbonate minerals.

Interestingly, the c/c_0 ratios exhibit a more diverged feature than the a/a_0 ratios (Fig. 5). This intrinsically reflects the MO_6 octahedra (M = Ca, Mn, Fe, and Mg) are more compressible than the CO_3^{2-} units. $MnCO_3$ has the greatest c/c_0 ratios at 0–15 GPa at room temperature (Liu et al. 2016; Palaich et al. 2015). However, this tendency is changed with increasing pressure (Fig. 5). In particular, $MnCO_3$ and $(Mg,Fe)CO_3$ single-divalent metal carbonates have nearly the same c/c_0 ratios at 15–20 GPa. Moreover, unlike the a/a_0 ratios of these carbonates, the c/c_0 ratios of single-divalent metal carbonates appear to be much larger than that of double carbonates under high pressures (Fig. 5). In principle, the larger effective cation radius features longer bonding lengths and weaker interactions between the CO_3^{2-} group and metal cations (Hazen et al. 2000). In particular, the *c* axial compressibility of those carbonates are highly correlated to the effective cation radii in the MO_6 octahedral configuration under high pressures. As in manganese dolomite, Mn^{2+} can largely substitute Ca^{2+}, and the *c*-axis compressibility is significantly affected by the coexisting MnO_6 and CaO_6 octahedra with different sizes and distortion/rotation in the same layer.

By the same logic, the c/a ratios are also sensitive to the relative size of effective cation radii in carbonates, as shown in Figure 6. The difference in the c/a ratios could be as large as 5% between calcite and magnesite (Fiquet and Reynard 1999; Redfern and Angel 1999). Notably, the c/a ratios of manganese dolomite lie between calcite and magnesite at ambient conditions. Additionally, the difference in the c/a ratios between single and double carbonates decreases with increasing pressure, principally ascribed to the relatively greater compressibility of CaO_6 octahedra along the *c* axis, with respect to MnO_6, MgO_6 and FeO_6 octahedra under high pressures (Palaich et al. 2015). Meanwhile, MO_6 octahedra may distort and rotate with increasing pressure, as demonstrated by the c/a ratio slope of carbonates (Fig. 7). Except magnesite ($MgCO_3$), other single-divalent metal carbonates remain a relatively stable and low slope with increasing pressure (Palaich et al. 2015). Remarkably, double carbonates feature abrupt changes in the c/a ratio slope, likely associated with the extent of MO_6 octahedral distortion and rotation (Fig. 7). It is worth noting that both the Ca111 and Ca76 show a dramatic change in the c/a ratio slope at ~8 GPa, which might be an intrinsic high-pressure behavior common

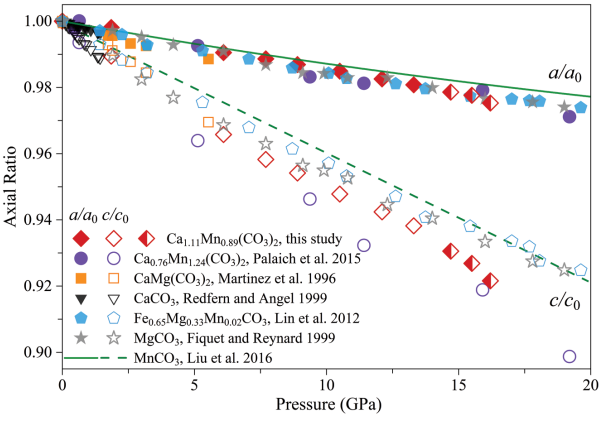

Figure 5. The axial ratios of carbonate minerals with increasing pressure at room temperature. Solid and open symbols represent a/a_0 and c/c_0, respectively. Error bars smaller than symbols are not shown for clarity. Note that the half-filled diamond symbols represent the values after diffraction splits of $Ca_{1.11}Mn_{0.89}(CO_3)_2$, which should be used with caution (see Table 1 for more details). (Color online.)

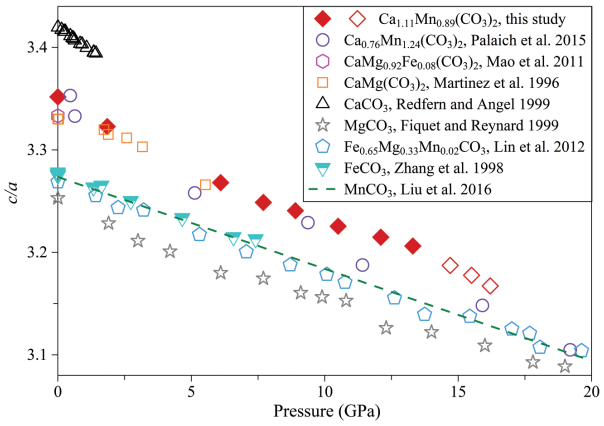

FIGURE 6. The *c*/*a* ratio values of carbonate minerals with increasing pressure at room temperature. Error bars smaller than symbols are not shown for clarity. Note that the open diamond symbols represent the values after diffraction splits of $Ca_{1.11}Mn_{0.89}(CO_3)_2$, which should be used with caution (see Table 1 for more details). (Color online.)

for manganese dolomite minerals upon compression at room temperature. Furthermore, Ca111 has the absolute values of the *c*/*a* ratio slope smaller than Ca76 at <13.3 GPa, reflecting that Ca111 is less compressible than Ca76 (Fig. 7).

The evolving distortion/rotation of CaO_6 and MnO_6 octahedra in the same layer may hold the key to decoding the splits of single-crystal diffraction spots observed in the Ca111 sample with increasing pressure (Fig. 2). The high-angle diffraction spots such as {128} became slightly elongated at 13.3 GPa while the low-angle diffraction spots were still pretty round (Fig. 2b). This difference reflects the lattice distortion is accumulating to be visible initially via the deformation of the high-angle diffraction spots. We note that the splits of the lattice modes were observed at pressures greater than 10.5 GPa in Raman spectra of the Ca111 sample when being compressed in neon (Wang et al. 2022). Compared with X-ray diffraction measurements, the use of the same pressure-transmitting medium indicates that laser Raman spectroscopy is a more sensitive probe to detect the lattice distortion of carbonates. Additionally, Wang et al. (2022) pointed out

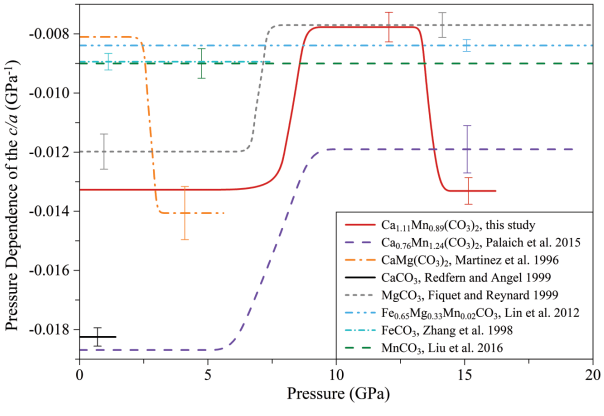

FIGURE 7. The *c*/*a* ratio slope of carbonate minerals with increasing pressure at room temperature. Vertical ticks represent one standard deviation of the *c*/*a* ratio slope values. (Color online.)

that the use of helium as a pressure-transmitting medium would postpone the splits of the lattice Raman modes to 13.7 GPa for the Ca111 sample. It is principally because deviatoric stress accumulates slower in helium than in neon. Upon further compression in neon, the splits of high-angle diffraction spots were visible at 14.7 GPa, while the splits of low-angle diffraction were until 17.5 GPa for the single-crystal Ca111 sample (Fig. 2c). This is largely due to the higher spatial resolutions at the higher angles in XRD patterns. The diffraction split magnitudes of {104}, {110}, and {116} planes are comparable to each other, and they could be as large as 0.040 ± 0.002 Å at 22.4 GPa (Fig. 2d).

The diffraction intensities dramatically decreased at 28.1 GPa and vanished with increasing pressure to 51.2 GPa. Such changes in diffraction intensities reflect the significant adjustments in the atomic positions of Ca^{2+} and Mn^{2+} for the Ca111 sample at pressures greater than 22.4–28.1 GPa. At the same time, the splits of the internal modes occur in the single-crystal Ca111's Raman spectra at ~24 GPa, including the symmetric stretching (ν_1), out-of-plane bending (ν_2) and in-plane bending (ν_4) (Wang et al. 2022). These internal Raman modes originate from vibrations of the CO_3^{2-} group. Thus, the reported Raman peak splits are intrinsically related to the dramatic changes in the bonding environments of the CO_3^{2-} group, corresponding to the dolomite-III phase of Ca111 assigned by Wang et al. (2022) approximately at 24–50 GPa. In other words, the dramatic adjustments in atomic positions not only break up the long-range order of the cation layers of MnO_6 and CaO_6, causing the blurred diffraction spots and vanished intensities, but also alter the bonding environments of the CO_3^{2-} group in the Ca111 sample at ≥24 GPa. In addition, the Ca111 sample features the splits of the lattice modes in Raman spectra at 13.3–22.4 GPa while the internal modes of the CO_3^{2-} group remain unaffected, corresponding to the dolomite-II phase in Wang et al. (2022).

Together with XRD results, Raman spectroscopic measurements indicate that the lattice distortion is mainly accumulated in the cation layers of CaO_6 and MnO_6 octahedra in the dolomite-II phase of Ca111. It appears to minimally influence the rigid CO_3^{2-} group. Moreover, Figures 2d–2e vividly demonstrate that Ca111 might contain two domains that were subjected to different lattice strains at 17.5 and 22.4 GPa. When the *d*-spacing difference between the two domains exceeded 0.040 Å at 28.1–51.2 GPa, no characteristic diffraction with moderate-strong intensities could be observed in the Ca111 sample (Figs. 2e–2f). Therefore, the dolomite-III phase has a lattice much more distorted than the dolomite-II phase for Ca111, as shown in Raman spectra collected by Wang et al. (2022). Additionally, those high-pressure phase transitions are reversible, and the recovered Ca111 sample did not feature the characteristic Raman peaks of $CaCO_3$ and $MnCO_3$ at ambient conditions, evidencing that the manganese dolomite would not decompose up to 60 GPa at room temperature.

IMPLICATIONS

Carbonates are key deep carbon-bearing phases in the Earth's interior, and it is essential to decode how carbonate structure evolves with respect to varying cations as pressure rises. Compared with the Ca76 sample investigated by Palaich et al. (2015), our Ca111 sample exhibits higher bulk moduli as its Ca^{2+} content is closer to the ideal manganese dolomite

Ca100 composition, having 50% cations to be Ca^{2+}. We note that there might be diffraction splits in the polycrystalline Ca76 at 11.4–19.1 GPa in Palaich et al. (2015). Polycrystalline X-ray diffraction patterns generally feature broadened peaks, which may conceal the diffraction splits. More importantly, diffraction splits may be a common high-pressure behavior of the dolomite group minerals. Santillán et al. (2003) reported the split and disappearance of X-ray diffraction peaks for polycrystalline $CaMg(CO_3)_2$ at pressures greater than ~20 GPa at room temperature, with a 16:3:1 mixture of methanol:ethanol:water serving as the pressure-transmitting medium. Compared with the Ca111 sample, the elevated transition pressure for $CaMg(CO_3)_2$ is mainly because the effective radius of Mg^{2+} is much smaller than that of Mn^{2+}. Similarly, the {104} and {116} diffraction peaks of polycrystalline $CaMg(CO_3)_2$ split into two components, and this doublet could remain stable approximately to 50 GPa at room temperature. Santillán et al. (2003) suggested that the dolomite-II phase of $CaMg(CO_3)_2$ likely has a doubled unit cell relative to the calcite-III structure, but this feature could not be well resolved based on their powder diffraction patterns. Here, with the help of single-crystal diffraction patterns, the splits of all diffraction spots of our manganese dolomite sample are highly related to the magnitude of lattice distortion (microstrain) accumulated with increasing pressure. Furthermore, Wang et al. (2022) revealed that the rigid CO_3^{2-} group in highly distorted $CaMg(CO_3)_2$ is subjected to more complex bonding environments than the Ca111 sample at 50 GPa and room temperature. In other words, chemical variations can modulate the bonding environments in the highly distorted dolomite group minerals under high pressures as illustrated in iron-bearing carbonates (Hu et al. 2023). The structural evolution of the dolomite group minerals can be further complicated when the distorted CaO_6 octahedra enter the regime of distorted polyhedra of CaO_n ($7 \leq n \leq 9$) (Binck et al. 2020).

Subducting slabs contain some amount of manganese-bearing carbonate minerals, considering that Mn substitution for Mg, Fe, and Ca is ubiquitous in natural minerals (Reeder and Dollase 1989; Rividi et al. 2010; Efthimiopoulos et al. 2017). Besides, inclusions in super-deep diamonds embrace manganese-bearing dolomite minerals, evidencing the undisputed presence of manganese-bearing carbonates in the deep mantle (Brenker et al. 2007; Logvinova et al. 2019). The incorporation of manganese into mantle carbonates may alter their structural evolution when exposed to deep mantle conditions. Thus far, the high-pressure polymorphs of (Mg,Fe)-dolomite have been considered to be potential carbon carriers in the deep mantle (Mao et al. 2011; Merlini et al. 2012). Mn^{2+} has an effective radius larger than Fe^{2+} and Mg^{2+} throughout the entire mantle pressures (Shannon 1976). Hence, the substitution by Mn^{2+} could exert a relatively larger chemical strain on the carbonate lattice, which would generally lower the phase transition pressure. Recently, Lv et al. (2021) proposed a reversal of carbonate-silicate cation exchange of Ca^{2+} and Mg^{2+} in cold slabs at lower-mantle conditions. However, it still remains unclear how the presence of Mn^{2+} influences the structural evolution of carbonate minerals and their interactions with mantle silicates. Further, high temperature plays an important role in the stability and dynamics of mantle carbonates and places another dimension to be constrained for decoding the deep carbon cycle (e.g., Boulard et al. 2011; Cerantola et al. 2017; Hou et al. 2019; Lv et al. 2021; Gui et al. 2023). It is worth noting that there is still no agreement on whether $MnCO_3$ decomposes into diamond under high temperatures at >12 GPa (Liu et al. 2001; Ono 2006). Therefore, further work is demanded to elucidate the nature and state of Mn-bearing carbonate minerals at lower-mantle conditions.

Acknowledgments and funding

We thank Chaoshuai Zhao, Xiaowan Su, and Fuyang Liu for their assistance in data collection and interpretation. This study is funded by the National Key Research and Development Program of China (2019YFA0708502) and the National Natural Science Foundation of China (42072052). The Department of Mineral Sciences, Smithsonian Institution is acknowledged for supplying the manganese dolomite sample (Kutnohorite, no. NMNH148722). We acknowledge the use of synchrotron X-ray diffraction at the 13BM-C of GSECARS, Advanced Photon Sciences, Argonne National Laboratory. GeoSoilEnviroCARS is supported by the National Science Foundation- Earth Sciences (EAR-1634415) and the Department of Energy-GeoSciences (DE-FG02-94ER14466). 13BM-C is partially supported by COMPRES under NSF Cooperative Agreement EAR-1606856. This research used resources of the Advanced Photon Source, a U.S. Department of Energy (DOE) Office of Science User Facility operated for the DOE Office of Science by Argonne National Laboratory under Contract No. DE-AC02-06CH11357. Some experiments are supported by the Synergic Extreme Condition User Facility (SECUF).

References cited

Binck, J., Chariton, S., Stekiel, M., Bayarjargal, L., Morgenroth, W., Milman, V., Dubrovinsky, L., and Winkler, B. (2020) High-pressure, high-temperature phase stability of iron-poor dolomite and the structures of dolomite-IIIc and dolomite-V. Physics of the Earth and Planetary Interiors, 299, 106403, https://doi.org/10.1016/j.pepi.2019.106403.

Boulard, E., Gloter, A., Corgne, A., Antonangeli, D., Auzende, A.L., Perrillat, J.P., Guyot, F., and Fiquet, G. (2011) New host for carbon in the deep Earth. Proceedings of the National Academy of Sciences of the United States of America, 108, 5184–5187, https://doi.org/10.1073/pnas.1016934108.

Brenker, F.E., Vollmer, C., Vincze, L., Vekemans, B., Szymanski, A., Janssens, K., Szaloki, I., Nasdala, L., Joswig, W., and Kaminsky, F. (2007) Carbonates from the lower part of transition zone or even the lower mantle. Earth and Planetary Science Letters, 260, 1–9, https://doi.org/10.1016/j.epsl.2007.02.038.

Cerantola, V., Bykova, E., Kupenko, I., Merlini, M., Ismailova, L., McCammon, C., Bykov, M., Chumakov, A.I., Petitgirard, S., Kantor, I., and others. (2017) Stability of iron-bearing carbonates in the deep Earth's interior. Nature Communications, 8, 15960, https://doi.org/10.1038/ncomms15960.

Dasgupta, R. and Hirschmann, M.M. (2010) The deep carbon cycle and melting in Earth's interior. Earth and Planetary Science Letters, 298, 1–13, https://doi.org/10.1016/j.epsl.2010.06.039.

Dera, P., Zhuravlev, K., Prakapenka, V., Rivers, M.L., Finkelstein, G.J., Grubor-Urosevic, O., Tschauner, O., Clark, S.M., and Downs, R.T. (2013) High pressure single-crystal micro X-ray diffraction analysis with GSE_ADA/RSV software. High Pressure Research, 33, 466–484, https://doi.org/10.1080/08957959.2013.806504.

Dorfman, S.M., Badro, J., Nabiei, F., Prakapenka, V.B., Cantoni, M., and Gillet, P. (2018) Carbonate stability in the reduced lower mantle. Earth and Planetary Science Letters, 489, 84–91, https://doi.org/10.1016/j.epsl.2018.02.035.

Efthimiopoulos, I., Jahn, S., Kuras, A., Schade, U., and Koch-Müller, M. (2017) Combined high-pressure and high-temperature vibrational studies of dolomite: Phase diagram and evidence of a new distorted modification. Physics and Chemistry of Minerals, 44, 465–476, https://doi.org/10.1007/s00269-017-0874-5.

Efthimiopoulos, I., Germer, M., Jahn, S., Harms, M., Reichmann, H.J., Speziale, S., Schade, U., Sieber, M., and Koch-Müller, M. (2019) Effects of hydrostaticity on the structural stability of carbonates at lower mantle pressures: The case study of dolomite. High Pressure Research, 39, 36–49, https://doi.org/10.1080/08957959.2018.1558223.

Farsang, S., Louvel, M., Zhao, C., Mezouar, M., Rosa, A.D., Widmer, R.N., Feng, X., Liu, J., and Redfern, S.A.T. (2021) Deep carbon cycle constrained by carbonate solubility. Nature Communications, 12, 4311, https://doi.org/10.1038/s41467-021-24533-7.

Fei, Y., Ricolleau, A., Frank, M., Mibe, K., Shen, G., and Prakapenka, V. (2007) Toward an internally consistent pressure scale. Proceedings of the National Academy of Sciences of the United States of America, 104, 9182–9186, https://doi.org/10.1073/pnas.0609013104.

Fiquet, G. and Reynard, B. (1999) High-pressure equation of state of magnesite: New data and a reappraisal. American Mineralogist, 84, 856–860, https://doi.org/10.2138/am-1999-5-619.

Gui, W., Shen, K., and Liu, J. (2023) Phase stability and reactions of subducting

$CaCO_3$ under upper mantle conditions. Acta Geologica Sinica—English Edition, 97, 309–315, https://doi.org/10.1111/1755-6724.15040.
Hammouda, T., Andrault, D., Koga, K., Katsura, T., and Martin, A.M. (2011) Ordering in double carbonates and implications for processes at subduction zones. Contributions to Mineralogy and Petrology, 161, 439–450, https://doi.org/10.1007/s00410-010-0541-z.
Hazen, R.M., Downs, R.T., and Prewitt, C.T. (2000) Principles of comparative crystal chemistry. Reviews in Mineralogy and Geochemistry, 41, 1–33, https://doi.org/10.2138/rmg.2000.41.1.
Hou, M., Zhang, Q., Tao, R., Liu, H., Kono, Y., Mao, H.K., Yang, W., Chen, B., and Fei, Y. (2019) Temperature-induced amorphization in $CaCO_3$ at high pressure and implications for recycled $CaCO_3$ in subduction zones. Nature Communications, 10, 1963, https://doi.org/10.1038/s41467-019-09742-5.
Hu, J., Xu, L., Liu, J., and Yue, D. (2023) Effects of spin transition and cation substitution on the optical properties and iron partitioning in carbonate minerals. Acta Geologica Sinica—English Edition, 97, 350–357, https://doi.org/10.1111/1755-6724.15042.
Kelemen, P.B., Matter, J., Streit, E.E., Rudge, J., Curry, W., and Blusztajn, J. (2011) Rates and mechanisms of mineral carbonation in peridotite: Natural processes and recipes for enhanced, *in situ* CO_2 capture and storage. Annual Review of Earth and Planetary Sciences, 39, 545–576, https://doi.org/10.1146/annurev-earth-092010-152509.
Klotz, S., Chervin, J.C., Munsch, P., and Le Marchand, G. (2009) Hydrostatic limits of 11 pressure transmitting media. Journal of Physics D: Applied Physics, 42, 075413, https://doi.org/10.1088/0022-3727/42/7/075413.
Kushiro, I. (1975) Carbonate-silicate reactions at high pressures and possible presence of dolomite and magnesite in the upper mantle. Earth and Planetary Science Letters, 28, 116–120, https://doi.org/10.1016/0012-821X(75)90218-6.
Lavina, B., Dera, P., Downs, R.T., Prakapenka, V., Rivers, M., Sutton, S., and Nicol, M. (2009) Siderite at lower mantle conditions and the effects of the pressure-induced spin-pairing transition. Geophysical Research Letters, 36, L23306, https://doi.org/10.1029/2009GL039652.
Lin, J.-F., Liu, J., Jacobs, C., and Prakapenka, V.B. (2012) Vibrational and elastic properties of ferromagnesite across the electronic spin-pairing transition of iron. American Mineralogist, 97, 583–591, https://doi.org/10.2138/am.2012.3961.
Liu, L.-G., Lin, C.-C., and Yang, Y.-J. (2001) Formation of diamond by decarbonation of $MnCO_3$. Solid State Communications, 118, 195–198, https://doi.org/10.1016/S0038-1098(01)00068-0.
Liu, J., Lin, J.-F., and Prakapenka, V.B. (2015) High-pressure orthorhombic ferromagnesite as a potential deep-mantle carbon carrier. Scientific Reports, 5, 7640, https://doi.org/10.1038/srep07640.
Liu, J., Caracas, R., Fan, D., Bobocioiu, E., Zhang, D., and Mao, W.L. (2016) High-pressure compressibility and vibrational properties of $(Ca,Mn)CO_3$. American Mineralogist, 101, 2723–2730, https://doi.org/10.2138/am-2016-5742.
Logvinova, A.M., Shatskiy, A., Wirth, R., Tomilenko, A.A., Ugap'eva, S.S., and Sobolev, N.V. (2019) Carbonatite melt in type Ia gem diamond. Lithos, 342–343, 463–467, https://doi.org/10.1016/j.lithos.2019.06.010.
Lv, M., Dorfman, S.M., Badro, J., Borensztajn, S., Greenberg, E., and Prakapenka, V.B. (2021) Reversal of carbonate-silicate cation exchange in cold slabs in Earth's lower mantle. Nature Communications, 12, 1712, https://doi.org/10.1038/s41467-021-21761-9.
Malusà, M.G., Frezzotti, M.L., Ferrando, S., Brandmayr, E., Romanelli, F., and Panza, G.F. (2018) Active carbon sequestration in the Alpine mantle wedge and implications for long-term climate trends. Scientific Reports, 8, 4740, https://doi.org/10.1038/s41598-018-22877-7.
Mao, Z., Armentrout, M., Rainey, E., Manning, C.E., Dera, P., Prakapenka, V.B., and Kavner, A. (2011) Dolomite III: A new candidate lower mantle carbonate. Geophysical Research Letters, 38, L22303, https://doi.org/10.1029/2011GL049519.
Martinez, I., Zhang, J., and Reeder, R.J. (1996) In situ X-ray diffraction of aragonite and dolomite at high pressure and high temperature: Evidence for dolomite breakdown to aragonite and magnesite. American Mineralogist, 81, 611–624, https://doi.org/10.2138/am-1996-5-608.
Merlini, M., Crichton, W.A., Hanfland, M., Gemmi, M., Müller, H., Kupenko, I., and Dubrovinsky, L. (2012) Structures of dolomite at ultrahigh pressure and their influence on the deep carbon cycle. Proceedings of the National Academy of Sciences of the United States of America, 109, 13509–13514, https://doi.org/10.1073/pnas.1201336109.
Merlini, M., Cerantola, V., Gatta, G.D., Gemmi, M., Hanfland, M., Kupenko, I., Lotti, P., Müller, H., and Zhang, L. (2017) Dolomite-IV: Candidate structure for a carbonate in the Earth's lower mantle. American Mineralogist, 102, 1763–1766, https://doi.org/10.2138/am-2017-6161.
Morlidge, M., Pawley, A., and Droop, G. (2006) Double carbonate breakdown reactions at high pressures: An experimental study in the system CaO-MgO-FeO-MnO-CO_2. Contributions to Mineralogy and Petrology, 152, 365–373, https://doi.org/10.1007/s00410-006-0112-5.
Ono, S. (2006) High-pressure phase transformation in $MnCO_3$: A synchrotron XRD study. Mineralogical Magazine, 71, 105–111, https://doi.org/10.1180/minmag.2007.071.1.105.
Palaich, S.E.M., Heffern, R.A., Watenphul, A., Knight, J., and Kavner, A. (2015) High-pressure compressibility and phase stability of Mn-dolomite (kutnohorite). American Mineralogist, 100, 2242–2245, https://doi.org/10.2138/am-2015-5095.
Plank, T. and Manning, C.E. (2019) Subducting carbon. Nature, 574, 343–352, https://doi.org/10.1038/s41586-019-1643-z.
Prescher, C. and Prakapenka, V.B. (2015) DIOPTAS: A program for reduction of two-dimensional X-ray diffraction data and data exploration. High Pressure Research, 35, 223–230, https://doi.org/10.1080/08957959.2015.1059835.
Redfern, S.A.T. (2000) Structural variations in carbonates. Reviews in Mineralogy and Geochemistry, 41, 289–308, https://doi.org/10.2138/rmg.2000.41.10.
Redfern, S.A.T. and Angel, R.J. (1999) High-pressure behaviour and equation of state of calcite, $CaCO_3$. Contributions to Mineralogy and Petrology, 134, 102–106, https://doi.org/10.1007/s004100050471.
Reeder, R.J. and, Dollase, W.A. (1989) Structural variation in the dolomite-ankerite solid-solution series: An X-ray, Mössbauer, and TEM study. American Mineralogist, 74, 1159–1167.
Rividi, N., van Zuilen, M., Philippot, P., Ménez, B., Godard, G., and Poidatz, E. (2010) Calibration of carbonate composition using micro-Raman analysis: Application to planetary surface exploration. Astrobiology, 10, 293–309, https://doi.org/10.1089/ast.2009.0388.
Sanchez-Valle, C., Ghosh, S., and Rosa, A.D. (2011) Sound velocities of ferromagnesian carbonates and the seismic detection of carbonates in eclogites and the mantle. Geophysical Research Letters, 38, L24315, https://doi.org/10.1029/2011GL049981.
Santillán, J., Williams, Q., and Knittle, E. (2003) Dolomite-II: A high-pressure polymorph of $CaMg(CO_3)_2$. Geophysical Research Letters, 30, 1054, https://doi.org/10.1029/2002GL016018.
Shannon, R.D. (1976) Revised effective ionic radii and systematic studies of interatomic distances in halides and chaleogenides. Acta Crystallographica Section A: Crystal Physics, Diffraction, Theoretical and General Crystallography, 32, 751–767, https://doi.org/10.1107/S0567739476001551.
Shcheka, S.S., Wiedenbeck, M., Frost, D.J., and Keppler, H. (2006) Carbon solubility in mantle minerals. Earth and Planetary Science Letters, 245, 730–742, https://doi.org/10.1016/j.epsl.2006.03.036.
Shen, G., Wang, Y., Dewaele, A., Wu, C., Fratanduono, D.E., Eggert, J., Klotz, S., Dziubek, K.F., Loubeyre, P., Fat'yanov, O.V., and others. (2020) Toward an international practical pressure scale: A proposal for an IPPS ruby gauge (IPPS-Ruby2020). High Pressure Research, 40, 299–314, https://doi.org/10.1080/08957959.2020.1791107.
Wang, F., Zhao, C., Xu, L., and Liu, J. (2022) Effects of hydrostaticity and Mn-substitution on dolomite stability at high pressures. American Mineralogist, 107, 2234–2241, https://doi.org/10.2138/am-2022-8248.
Zhang, J., Martinez, I., Guyot, F., and Reeder, R.J. (1998) Effects of $Mg\text{-}Fe^{2+}$ substitution in calcite-structure carbonates: Thermoelastic properties. American Mineralogist, 83, 280–287, https://doi.org/10.2138/am-1998-3-411.
Zhao, C., Xu, L., Gui, W., and Liu, J. (2020) Phase stability and vibrational properties of iron-bearing carbonates at high pressure. Minerals, 10, 1142, https://doi.org/10.3390/min10121142.
Zhao, C., Lv, C., Xu, L., Liang, L., and Liu, J. (2021) Raman signatures of the distortion and stability of $MgCO_3$ to 75 GPa. American Mineralogist, 106, 367–373, https://doi.org/10.2138/am-2020-7490.

Manuscript received January 28, 2023
Manuscript accepted May 13, 2023
Accepted manuscript online May 25, 2023
Manuscript handled by Zhicheng Jing